Chemical Science

ROYAL SOCIETY OF CHEMISTRY

EDGE ARTICLE

View Article Online
View Journal | View Issue

Cite this: *Chem. Sci.*, 2025, **16**, 16168

All publication charges for this article have been paid for by the Royal Society of Chemistry

Dual-emissive self-reporting photosensitizers characterized by Kasha/*anti*-Kasha behaviors engineered *via* a gradient donor–acceptor strategy

Xixin Gu, †[a] Xinyi Zhang, †[a] Yujie Han,[b] Ju Mei, *[a] Qi-Wei Zhang *[b] and Jianli Hua *[a]

Real-time monitoring of photodynamic therapy (PDT) is essential for precision medicine, yet remains hindered by microenvironmental interference and photobleaching of conventional mono-emissive photosensitizers (PSs). Herein, inspired by the energy level gradients depicted in the Jablonski diagram, we report a gradient donor–acceptor molecular design strategy to overcome Kasha's rule, achieving intrinsic dual-emissive PSs. Combining femtosecond transient absorption spectroscopy with theoretical calculations, we have verified the Kasha/*anti*-Kasha properties of the compounds: near-infrared (NIR) emission peaking at 710 nm, exhibiting viscosity dependence stems, from the S_1-to-S_0 excited-state decay of the primary acceptor–donor framework, whereas visible emission at 530–590 nm, significantly enhanced upon DNA binding, originates from the S_2-to-S_0 excited-state decay of the additional acceptor–donor segment. A systematic comparison of the effects of additional acceptors on *anti*-Kasha behaviors and photogenerated reactive oxygen species (ROS) performance has been conducted by constructing two diketopyrrolopyrrole (DPP)-based isomers, namely **DPP-F32** and **DPP-F34**. Both PSs target the Golgi apparatus to activate NIR signals, but only **DPP-F32** exhibits visible emission in the nucleus of apoptotic cells, enabling ratiometric tracking of the PDT process at two-/three-dimensional cellular models *via* dual-channel imaging. This study provides a new paradigm for self-reporting PSs with Kasha/*anti*-Kasha behaviors that combine precise targeting, efficient ROS generation, and real-time dynamic monitoring.

Received 28th May 2025
Accepted 31st July 2025

DOI: 10.1039/d5sc03880d

rsc.li/chemical-science

Introduction

Photodynamic therapy (PDT), characterized by its minimally invasive nature, high spatiotemporal precision, and controllability, has emerged as a cutting-edge modality in tumor-targeted precision medicine.[1–3] The advancement of PDT hinges critically on the development of photosensitizers (PSs) that simultaneously achieve efficient tumor targeting, deep-tissue penetration, and robust ROS generation.[4–6] Conventional PSs induce cell apoptosis through ROS production while enabling lesion localization *via* fluorescence (FL) imaging.[7] Capitalizing on the superior spatial resolution and real-time visualization ability of FL imaging, FL imaging-guided PDT theranostics has garnered significant attention.[8,9] However, current PDT protocols lack capacity for early therapeutic response assessment, relying instead on conventional imaging techniques such as magnetic resonance imaging (MRI) or computed tomography (CT) to monitor tumor volume changes.[10–12] These methods suffer from insufficient sensitivity/specificity and potential radiation hazards,[13,14] underscoring the urgent need for FL-based real-time *in situ* monitoring of cellular activity to optimize light dosage regulation and prognostic evaluation.

Correspondingly, the development of self-reporting PSs to achieve precise treatment and tumor stratification has drawn widespread interest.[15–18] For instance, Tang's group developed PSs capable of translocating from mitochondria to the nucleus during PDT-induced apoptosis.[19] Zhang's group successfully designed self-reporting PSs that migrate from the cell membrane to the nucleus of drug-resistant tumors during PDT and provided guidance for clinical chemotherapeutic drug selection.[20] Nevertheless, mono-emissive probes are prone to being afflicted with microenvironmental interference, which complicates signal interpretation.[21,22] In contrast, dual-emissive probes facilitate ratiometric imaging that not only dynamically monitors cell viability changes but also eliminates staining/experimental artifacts.[23–25] Although Förster resonance energy

[a]*Key Laboratory for Advanced Materials and Joint International Research Laboratory for Precision Chemistry and Molecular Engineering, Feringa Nobel Prize Scientist Joint Research Center, Frontiers Science Center for Materiobiology and Dynamic Chemistry, School of Chemistry and Molecular Engineering, East China University of Science and Technology, 130 Meilong Road, Shanghai 200237, P. R. China. E-mail: daisymeiju@ecust.edu.cn; jlhua@ecust.edu.cn*

[b]*Shanghai Key Laboratory of Green Chemistry and Chemical Processes, Department of Chemistry, School of Chemistry and Molecular Engineering, East China Normal University, Shanghai 200241, P. R. China. E-mail: qwzhang@chem.ecnu.edu.cn*

† Contributed equally to this work.

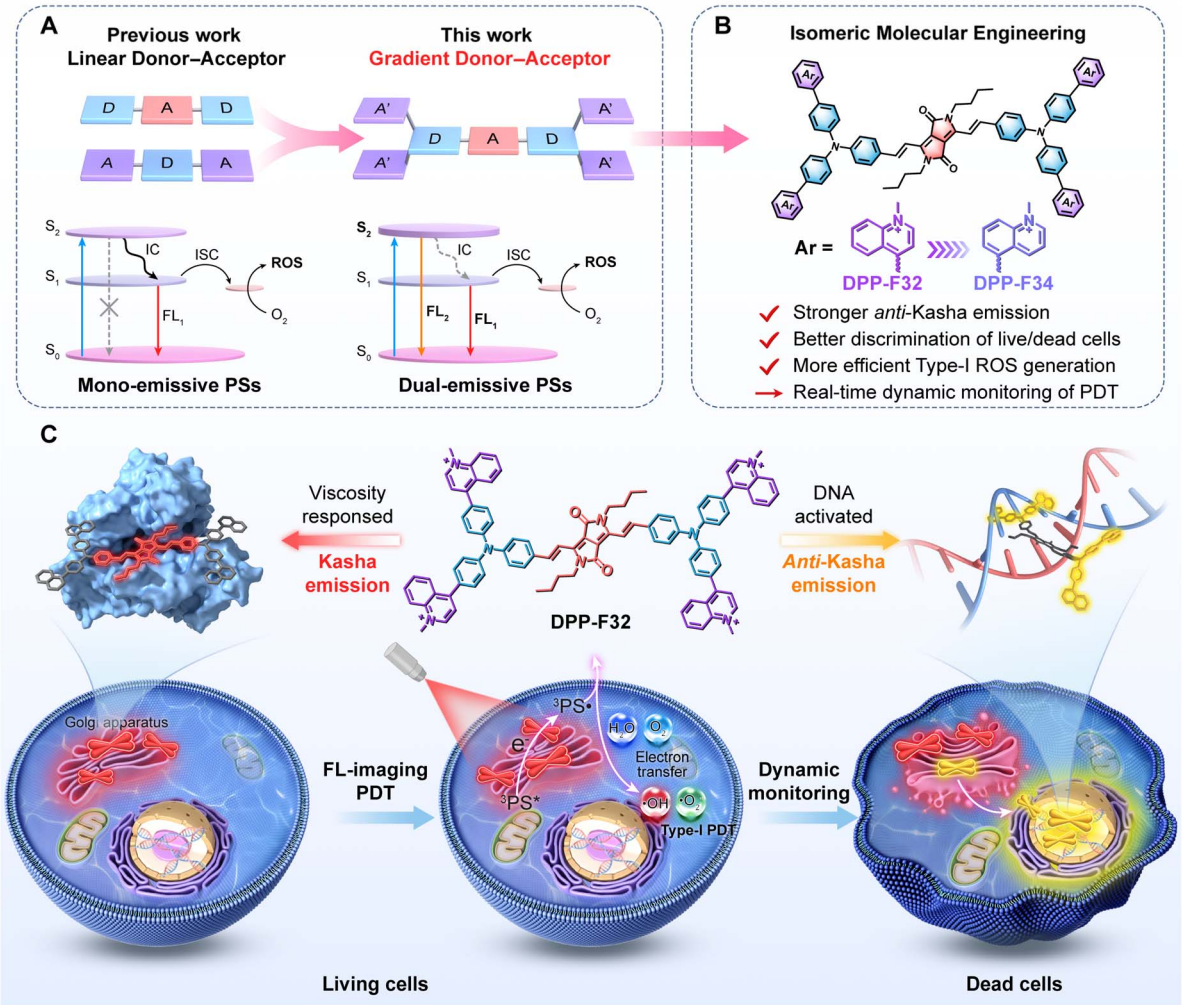

Scheme 1 (A) The gradient D–A structure facilitates the construction of dual-emissive PSs with *anti*-Kasha/Kasha behaviors. (B) Precise regulation through additional acceptor engineering. (C) Dual responses of **DPP-F32** to DNA and viscosity for distinguishing live/dead cells and ratiometric monitoring of dynamic PDT.

transfer (FRET) probes and reactive unimolecular ratiometric systems offer potential solutions, limitations such as excitation/emission crosstalk and differential photobleaching hinder their broad application.[26,27] Strategies for developing single-molecular probes with intrinsic dual-emissive properties are more promising.[28,29]

Limited by Kasha's rule,[30] the overwhelming majority of all the organic light-emitting materials exhibit only a single emission band originating from the lowest-energy electronic excited state. Despite this, recent reports have revealed new breakthroughs.[31–34] From the perspective of molecular assembly, by combining several emissive building blocks in one molecule and hindering the energy transfer among them, it is possible to break Kasha's rule and achieve multiple emissions under ambient conditions.[35] To achieve *anti*-Kasha emission and reliable ratiometric bioimaging of biomolecules such as glutathione (GSH) and cysteine (Cys), Guo's group enlarged the S_2–S_1 energy gap by integrating fluorescein and chromene building blocks with dicyanomethylene-4*H*-pyran (DCM-IFC).[36] Subsequently, Tang's group discovered that the introduction of electron donors with varying strengths into the conjugated system enables modulation of the internal conversion rates among corresponding excited states, leading to the development of *anti*-Kasha molecular probes capable of detecting the polarity of the cellular microenvironment.[37] Based on the D–π–A design, Feng's group successfully constructed PSs with *anti*-Kasha characteristics, achieving lipid droplet- and mitochondria-targeted dual-fluorescence imaging-guided PDT.[38] Inspired by a series of studies on organic luminescent materials exhibiting *anti*-Kasha behavior and their biological applications (Table S1), PSs with *anti*-Kasha behaviors perhaps enable real-time monitoring of cellular dynamics during PDT through dual-emissive functionality, wherein one emission provides subcellular localization references and the other indicates target interactions correlated with cell death progression. However, self-reporting PSs integrating these functionalities still remain unexplored.

Although D–A–D or A–D–A molecular architectures enhance photosensitization efficiency, the linear mode of charge transfer makes them typically exhibit mono-emission characteristics and encounter fundamental challenges in overcoming Kasha's rule.[39,40] To address this limitation, herein, we have developed a gradient D–A (*i.e.*, dA′–D–A–D–dA′, where dA′ denotes an additional electron acceptor, D denotes the electron donor, and A denotes the primary electron acceptor) engineering strategy that integrated both D–A–D and A′–D–A′ configurations into a single molecule, in which the electron-withdrawing capacity of A′ should be significantly weaker than that of A.

This integration aims to preserve their photosensitization capabilities and achieve double excited-state emissions through a spatially separated charge transfer pathway (Scheme 1A). As a proof of concept, two diketopyrrolopyrrole (DPP)-based isomers, **DPP-F32** and **DPP-F34** (Scheme 1B), were constructed using the 3,6-divinyl-substituted diketopyrrolopyrrole derivative as the core backbone and methylquinolinium as functional units and additional acceptors.[41] Photophysical characterization revealed that **DPP-F32** and **DPP-F34** display distinct dual absorption and dual emission properties in high-polarity solvents, with their *anti*-Kasha behaviors being corroborated by femtosecond transient absorption spectroscopy and theoretical calculations. Notably, the Kasha emission in the NIR region exhibited viscosity-dependent behavior, while the *anti*-Kasha emission in the visible region showed significant enhancement upon DNA binding. These observations were further verified by a series of theoretical calculations, including density functional theory calculations, molecular docking, and molecular dynamics simulations. Cellular imaging demonstrated NIR emission localization in the Golgi apparatus of living cells for both compounds, with negligible visible emission. In dead cells, **DPP-F32** specifically illuminated nuclei with visible emission while maintaining cytoplasmic NIR emission. In addition, compared with **DPP-F34**, **DPP-F32** exhibited a stronger ability to generate ROS, due to the stronger spin–orbit coupling (SOC) and more efficient electron transfer process in the type-I PDT pathway of *para*-substituted methylquinolinium. Most importantly, **DPP-F32** enabled dual-emissive ratiometric monitoring of the dynamic PDT process (Scheme 1C).

Results and discussion

Molecular design and synthesis

Vinyl DPP demonstrated superior type-I ROS generation capability compared to aryl DPP, with emission extending into the NIR region.[41,42] Molecules containing multiple methylpyridinium groups can intercalate into DNA grooves and translocate from the cytoplasm to the nucleus during apoptosis.[18–20,43–46] To combine the advantages of the above two, we designed and synthesized two isomeric compounds, *i.e.*, **DPP-F32** and **DPP-F34** (Fig. 1A), incorporating triphenylamine as an electron donor as well as a bridge to connect vinyl DPP (primary acceptor) and methylquinolinium units (additional acceptors). Compared to methylquinolinium, vinyl DPP has a stronger electron-withdrawing capacity, and the distorted aniline structure spatially separates the charge transfer pathway between the two types of acceptors, which promotes the delocalization of dA′–D–A–D–dA′ into A–D–A and D–A–D structures. This is likely to facilitate the formation of PSs with enhanced multiple absorption and emission bands. The rationale for selecting *para*- and *meta*-substituted methylquinolinium units as two isomeric additional acceptors lies in their identical formula but distinct electron push–pull effects stemming from the position of substitution.

The synthetic routes to **DPP-F32** and **DPP-F34** are detailed in the SI (Scheme S1). Initially, the two substituted quinoline groups were conjugated to the triphenylamine group *via* Suzuki–Miyaura coupling. Subsequently, the quinoline-substituted TPA and the methyl DPP moieties were coupled through Knoevenagel condensation catalyzed by piperidine. Finally, the cationic products were obtained *via* nucleophilic substitution with methyl iodide. The targeted compounds and some key intermediates were fully characterized by ^{1}H NMR, ^{13}C NMR and high-resolution mass spectrometry (Fig. S1–S18).

Photophysical properties

To evaluate the solubility of **DPP-F32** and **DPP-F34**, the lipophilic-hydrophilic partition coefficient (log *P*) was determined using the direct measurement method. The log *P* values were found to be −2.19 for **DPP-F32** and −1.32 for **DPP-F34** (Fig. S19 and S20), indicating that their lipophilicity is higher than their hydrophilicity. Given their high polarity, the absorption spectra of **DPP-F32** and **DPP-F34** were subsequently measured in high-polarity solvents. As shown in Fig. S21, **DPP-F32** and **DPP-F34** exhibited excellent dual-absorption performance in the visible spectral range. Specifically, **DPP-F32** displayed absorption peaks at 480 nm ($\varepsilon = 4.76 \times 10^4$ L mol^{-1} cm^{-1}) and 620 nm ($\varepsilon = 6.97 \times 10^4$ L mol^{-1} cm^{-1}) in water. In contrast, **DPP-F34** exhibited a weaker first absorption peak at 470 nm ($\varepsilon = 2.41 \times 10^4$ L mol^{-1} cm^{-1}) and a second absorption peak at 620 nm ($\varepsilon = 5.74 \times 10^4$ L mol^{-1} cm^{-1}) in water. Considering the dual-absorption capability of **DPP-F32** and **DPP-F34** in highly polar solvents, we measured their fluorescence spectra at two excitation wavelengths (λ_{ex} = 450 nm and 610 nm). As shown in Fig. S22 and S23, both **DPP-F32** and **DPP-F34** exhibited quenching in water and distinct dual-emission in dimethyl sulfoxide (DMSO) and dimethylformamide (DMF), while merely mono-emission in ethanol (EtOH) and methanol (MeOH), suggesting that the two emission bands were affected by different factors.

Consequently, we chose DMSO as a solvent to more carefully investigate the absorption and emission performance of **DPP-F32** and **DPP-F34**. As depicted in Fig. 1B and E, the two emission bands observed in the fluorescence spectra corresponded to the two excitation peaks at 480 nm ($S_0 \rightarrow S_2$) and 625 nm ($S_0 \rightarrow S_1$), respectively, which aligned with the shape of the absorption peaks. Notably, **DPP-F32** and **DPP-F34** did not follow the classical empirical rule of emission, which is called Kasha's rule. Additionally, the dual-emission with *anti*-Kasha characteristics was also strongly supported by femtosecond time-resolved transient absorption spectroscopic (fs-TAS) experiments (Fig. S24). As shown in Fig. 1C and F, two ground-state

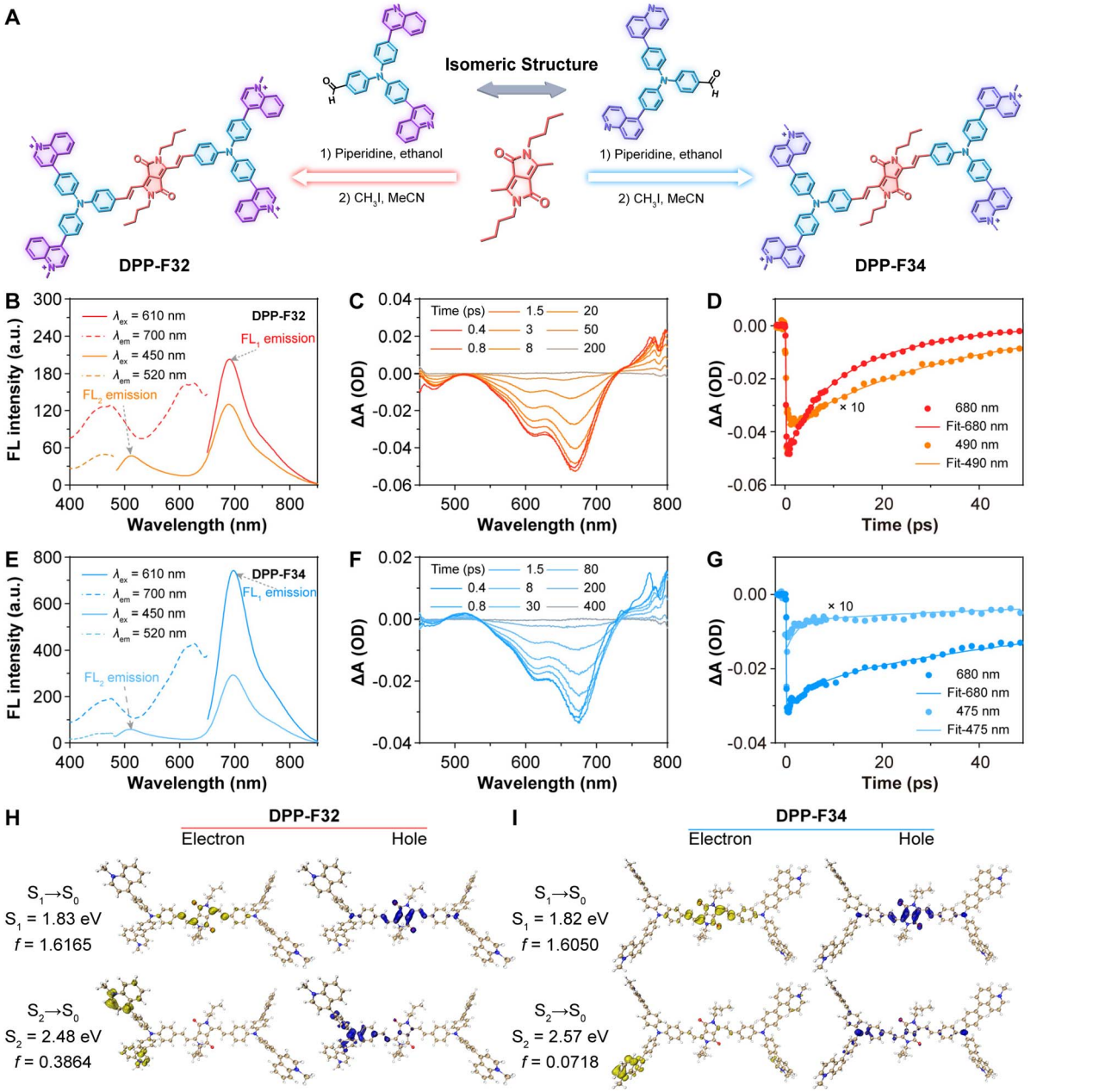

Fig. 1 (A) Synthetic routes to **DPP-F32** and **DPP-F34**. Excitation spectra (dotted lines, monitored at $\lambda_{em} = 520$ and 700 nm) and emission spectra (solid lines, excited at $\lambda_{ex} = 450$ and 610 nm) of **DPP-F32** (B) and **DPP-F34** (E) in DMSO. Representative selection of fs-TAS of **DPP-F32** (C) and **DPP-F34** (F) at different delay times after excitation at 450 nm in DMSO. A comparison of the transient absorption kinetics at different wavelengths of **DPP-F32** (D) and **DPP-F34** (G). Quantum chemical calculations and electron–hole analysis involved during the photoexcitation of **DPP-F32** (H) and **DPP-F34** (I).

bleaching (GSB) peaks at 480 nm and 625 nm were observed in the fs-TAS spectra of **DPP-F32** and **DPP-F34**, indicating that the two excited states originated from the same compound rather than impurities. The GSB peak of **DPP-F34** at 480 nm was weaker than that of **DPP-F32** due to a lower population in the second excited state. It is worth noting that the inflection point observed at 510 nm could be attributed to the offset of excited-state absorption (ESA) and stimulated emission (SE) from the second excited state (S_2), while the stronger negative peak at 680 nm arises from the superposition of GSB and SE from the first electronically excited singlet state (S_1), conclusively implying that **DPP-F32** and **DPP-F34** each have two emission states. More detailed information was obtained by monitoring the ultrafast kinetics dynamics of the compounds at 490 nm (for **DPP-F32**) or 475 nm (for **DPP-F34**), and 680 nm under excitation at 450 nm (Fig. 1D, G and Table S2). The negative amplitudes on both time scales exhibited by S_2 could be attributed to the ground state recovery ($t_1 = 33.8$ ps for **DPP-F32**, 23 ps for **DPP-F34**) and the fast relaxation process ($t_2 = 0.2$ ps), whereas the positive amplitudes in S_1 exhibited the same lifetime as in S_2,

which is perhaps attributed to the energy transfer process (internal conversion, IC) from the S_2 to the S_1 state. Importantly, the absolute values of the amplitudes of the higher excited states reflected the effective competition between $S_2 \rightarrow S_0$ ($\sim$0.22) and $S_2 \rightarrow S_1$ ($\sim$0.78).

To gain a deeper insight into the principles underlying *anti*-Kasha *versus* Kasha emissions for **DPP-F32** and **DPP-F34** in DMSO, we conducted systematic quantum chemical calculations (Table S3). The theoretical calculations demonstrated strong agreement with the experimental data, as evidenced by the two emission bands from the S_1 state (about 680 nm) and the S_2 state (about 490 nm), respectively. Notably, the two excited states were characterized by a large energy gap. The value of ΔE_{S2-S1} for **DPP-F32** and **DPP-F34** is 0.6463 eV (around 5200 cm^{-1}) and 0.7463 eV (around 6000 cm^{-1}), respectively. Such significant energy differences effectively suppress IC from the S_2 state to the S_1 state. Additionally, as shown in Fig. 1H and I, electron–hole analysis revealed that the electron distribution in the S_2 state was significantly localized within the methylquinolinium fragment, whereas the electron in the S_1 state primarily resided in the vinyl DPP fragment. Based on these observations, it can be inferred that the D–A–D configuration exhibited the Kasha emission (FL_1, NIR region), while the A′–D–A′ configuration conformed to the *anti*-Kasha emission (FL_2, visible region). Among them, the $S_2 \rightarrow S_0$ decay for **DPP-F32** exhibited a greater vibronic intensity ($f = 0.3864$), suggesting that stronger localized electron push–pull effects are more favorable for *anti*-Kasha behavior.

Luminescence behaviors and mechanism of DNA recognition

To date, regulating *anti*-Kasha behavior and effectively controlling emission from higher excited states are still great challenges, which substantially hinder the application of such molecules in optical imaging and biosensing. Considering multiple rotatory groups and D–A effects of **DPP-F32** and **DPP-F34**, which may give rise to the viscosity-responsiveness,[47,48] we conducted the verification experiments in the glycerol/DMSO mixtures. The FL intensity of **DPP-F32** and **DPP-F34** in the NIR region increased with the rising proportion of glycerol under excitation at both 450 nm and 610 nm (Fig. 2A, B, and S25), indicating that their NIR emission was predominantly modulated by viscosity. The intensity ratios of FL_1 excited by the two different wavelengths were equivalent and significantly higher than those of FL_2 (Fig. S26), suggesting that a high-viscosity environment facilitates Kasha emission. To verify whether the interaction between positively charged methylquinolinium salts and negatively charged substances could lead to the emission enhancement, we screened a series of negatively charged macromolecules including bovine serum albumin (BSA), heparin, polyacrylic acid (PAA), polyinosinic:polycytidylic acid (Poly I:C), polyinosinic acid (Poly I), polycytidylic acid (Poly C), yeast RNA, and CT DNA with identical molar masses (Fig. S27 and S28). Delightedly, the addition of CT DNA resulted in the strongest fluorescence signal. As illustrated in Fig. 2C, D, and S29, the FL intensity of **DPP-F32** and **DPP-F34** in the visible region gradually increased with increasing amount of CT DNA, while only weak signals of FL_1 were exhibited at both excitation wavelengths. Notably, upon the addition of CT DNA at a concentration of 120 μg mL^{-1}, the FL intensity of **DPP-F32** in the visible region was enhanced by 19.6-fold (only 3.9-fold for **DPP-F34**), and the maximum emission peak red-shifted from 535 to 595 nm. In contrast, the intensity ratios of FL_1 hardly changed at both excitation wavelengths, indicating that the radiation attenuation from S_1 to S_0 was inhibited upon adding CT DNA. The above results suggested that, through rational molecular design, we successfully grafted two distinct modules—Kasha emission (FL_1, S_1-to-S_0 transition) and *anti*-Kasha emission (FL_2, S_2-to-S_0 transition) onto a single molecule. Importantly, these two modules exhibited significant advantages (Fig. 2E): (1) the two emission bands exhibit remarkable spectral separation, with Kasha emission in the NIR region facilitates deep-tissue imaging; (2) the intensity of FL_2 is enhanced upon DNA binding, whereas the intensity of FL_1 depends on the ambient viscosity, which facilitates the orthogonal detection of two or more biological species. To the best of our knowledge, these are the molecules of choice for engineering advanced molecular probes.

Unlike the single emission with a consistent Stokes shift observed for conventional dyes upon increased viscosity or DNA addition,[45,46] the *anti*-Kasha emissions of **DPP-F32** and **DPP-F34** were dramatically enhanced upon DNA binding, which piqued our interest. When CT DNA was added at a concentration of 120 μg mL^{-1}, the absorption spectra of **DPP-F32** and **DPP-F34** showed a decrease in intensity and a red shift in the wavelength, indicating structural alterations in these compounds following DNA binding (Fig. S30). The circular dichroism (CD) spectra revealed that after introducing 10 μM of **DPP-F32** and **DPP-F34** (Fig. S31), the positive peak at 276 nm (attributed to base stacking) and the negative peak at 247 nm (indicative of helicity) of CT DNA were significantly intensified, suggesting that both PSs can intercalate into the DNA groove.[44] When an excessive amount of **DPP-F32** and **DPP-F34** (30 μM each) was added, the positive and negative CD bands of CT DNA were markedly reduced, likely due to base destacking and unwinding caused by electrostatic interactions with polycationic molecules. To decipher the interaction mechanism between **DPP-F32** (or **DPP-F34**) and DNA, we retrieved the X-ray crystal structure data of nuclear DNA (PDB ID: 4awl) from the Protein Data Bank and performed molecular docking calculations using AutoDock 4.2 software. In Fig. 2F and S32, it was observed that **DPP-F32** and **DPP-F34** could embed within the DNA groove *via* electrostatic interactions between the methylquinolinium unit and DNA bases, together with hydrogen bonding between the imide unit and ribose, which agrees well with the experimental data of CD spectroscopy. The calculated binding energy of **DPP-F32** to 4awl (−10.62 kcal mol^{-1}) was lower than that of **DPP-F34** (−8.80 kcal mol^{-1}), suggesting that **DPP-F32** exhibited greater targeting capability to DNA (Table S4).

To acquire a profound understanding of the significant differences caused by the isomeric methylquinolinium, we conducted further molecular dynamics (MD) simulations. The conformations of DNA-ligand complexes, derived from molecular docking using AutoDock 4.2 software, along with the free

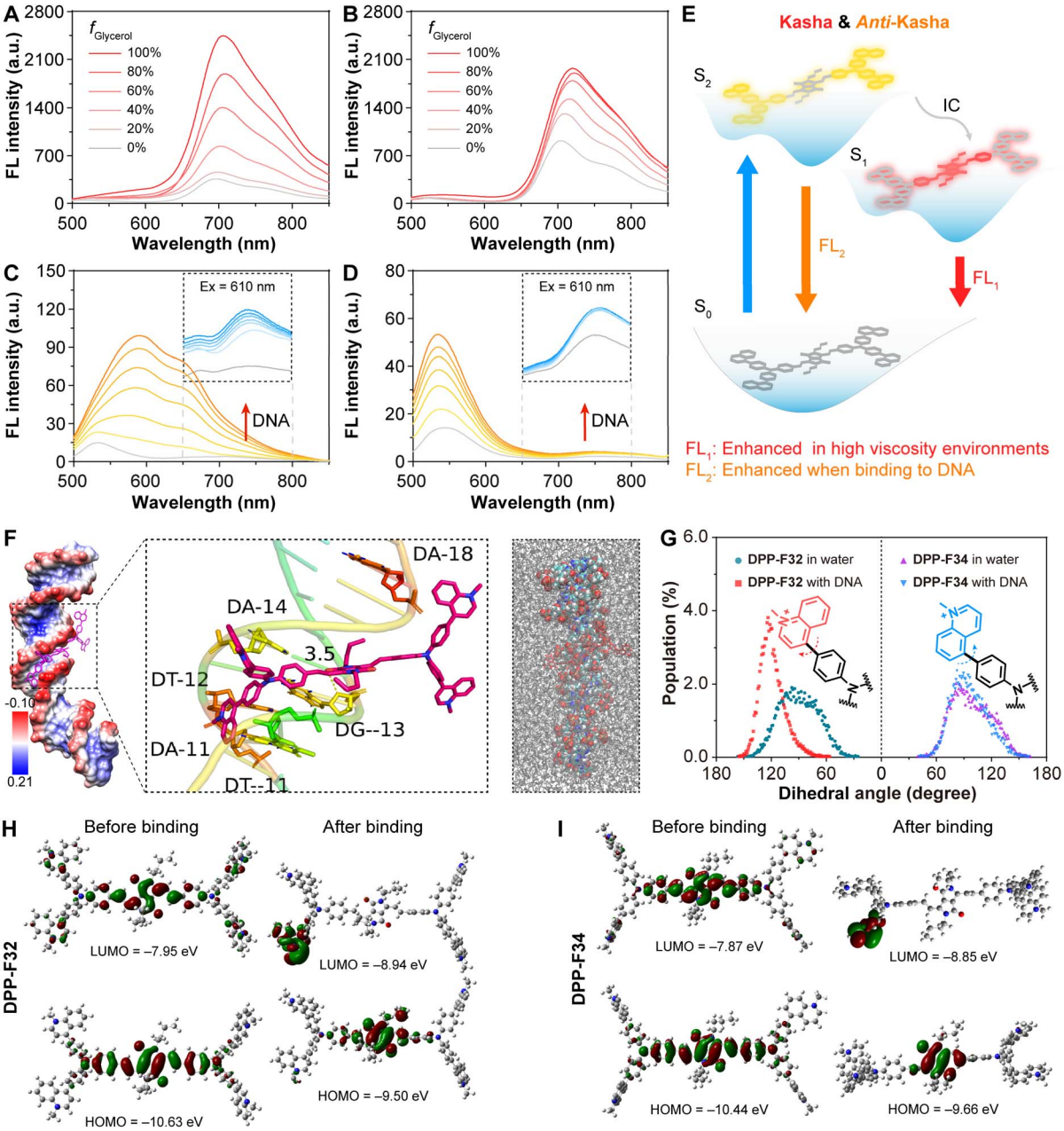

Fig. 2 FL spectra excited at λ_{ex} = 450 nm of **DPP-F32** (10 μM, A) and **DPP-F34** (10 μM, B) in glycerol/DMSO mixtures. FL spectra excited at λ_{ex} = 450 nm of **DPP-F32** (10 μM, C) and **DPP-F34** (10 μM, D) with the addition of various concentrations (0–120 μg mL^{-1}) of CT DNA. Inset: FL spectra excited at λ_{ex} = 610 nm. (E) Schematic illustration of *anti*-Kasha/Kasha emission. (F) Molecular docking calculation of DNA (4awl) with **DPP-F32** and molecular dynamics simulation snapshots of DNA-ligand complexes. The innermost molecules are shown in a space-filling model, while the other molecules are shown as rods. (G) Distributions of the representative dihedral angle of *para*-substituted or *meta*-substituted methylquinolinium groups. HOMO–LUMO distribution and the energy levels of **DPP-F32** (H) and **DPP-F34** (I) before and after binding to DNA.

ligands (**DPP-F32** and **DPP-F34**), were subjected to MD simulations in aqueous solution. The dihedral angles between the isomeric methylquinolinium unit and the adjacent benzene ring were calculated for comparison (Fig. 2G). In their unbound state, the wide distribution of dihedral angles for **DPP-F32** and **DPP-F34** indicated their free rotational flexibility. However, upon binding to DNA, the distribution of dihedral angles between the two methylquinolinium moieties and their adjacent phenyl rings became much narrower and shifted to the larger angle region, suggesting that the intramolecular motions of the methylquinolinium moiety were significantly restricted to induce the enhancement of FL_2. Notably, the dihedral angle distribution of **DPP-F32** changed dramatically from 60°–120° to 90°–150°, which is probably the reason for the red-shift of the *anti*-Kasha emission. Additionally, we calculated the highest occupied molecular orbital (HOMO) and the lowest unoccupied molecular orbital (LUMO) energy levels of **DPP-F32** and **DPP-F34** before and after binding to DNA (Fig. 3H and I). Compared to

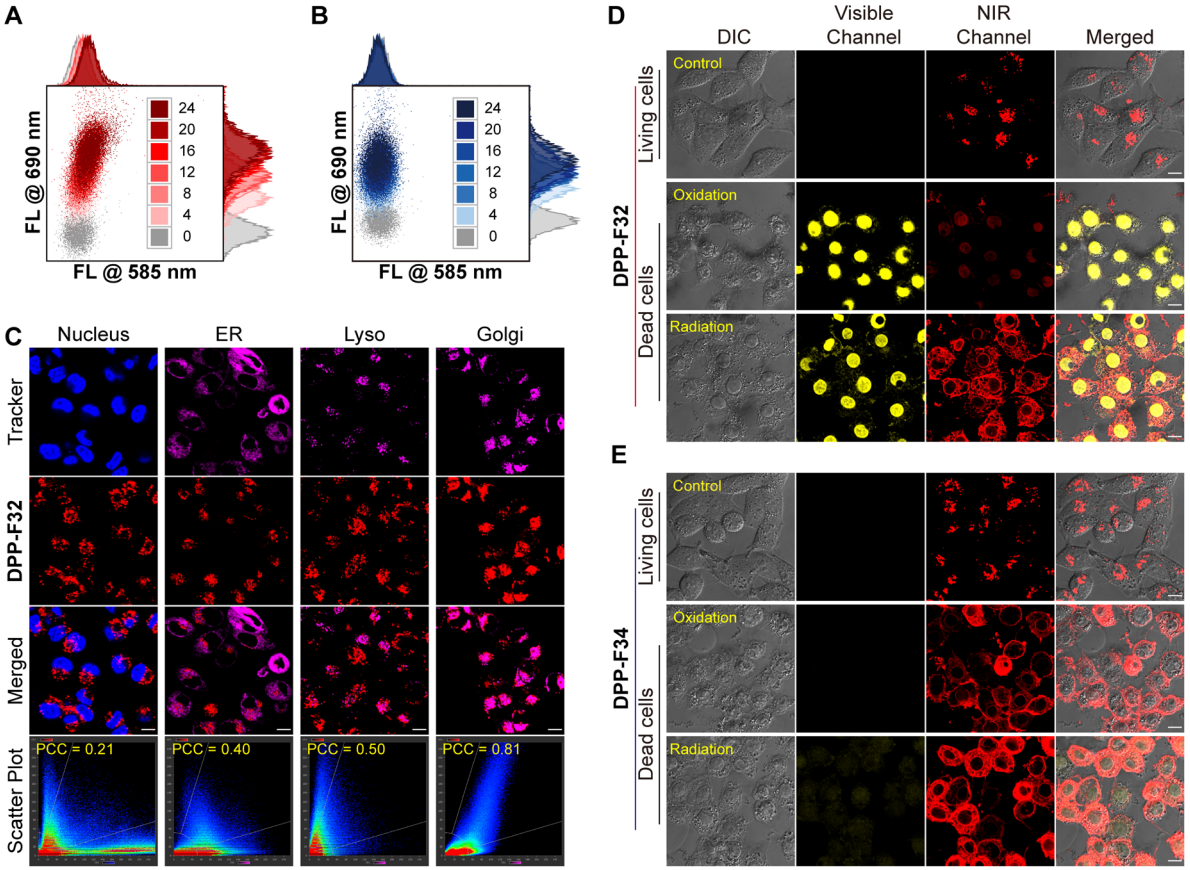

Fig. 3 Dual-channel flow cytometry dot-plot images of HeLa cells stained with **DPP-F32** (A) and **DPP-F34** (B) after incubation for different durations at a concentration of 10 μM. (C) Colocalization CLSM images of HeLa cells stained with **DPP-F32** (10 μM, $\lambda_{ex/em}$ = 638 nm/680–850 nm) and different commercial probes including Hoechst 33342 ($\lambda_{ex/em}$ = 405 nm/420–480 nm), ER-Tracker, Lyso-Tracker, and Golgi-Tracker ($\lambda_{ex/em}$ = 561 nm/580–650 nm). CLSM images of HeLa cells stained with **DPP-F32** (D) and **DPP-F34** (E) at a concentration of 10 μM under conditions of oxidative stress, ultraviolet irradiation, and no treatment. DIC: differential interference contrast. Scale bar: 10 μm.

the free state, the HOMO–LUMO energy gaps of **DPP-F32** and **DPP-F34** were significantly reduced upon DNA binding, facilitating electron transitions to higher excited states. Specifically, the electron clouds of the LUMO appeared to migrate from the main acceptor (A) to the auxiliary acceptor (dA′), promoting the population of the S_0-to-S_2 transition, which was consistent with the aforementioned electron–hole analysis. The smaller HOMO–LUMO gap of **DPP-F32** upon DNA binding (0.56 eV) as compared to that of **DPP-F34** (0.81 eV) under the parallel conditions also expounded the red-shift of the *anti*-Kasha emission of **DPP-F32.** In a word, the intramolecular motions of the methylquinolinium moiety were greatly hampered after binding to DNA, which propelled the population transfer from S_0 to S_2 while diminishing the population transfer from S_0 to S_1, thereby enhancing the *anti*-Kasha emission. This novel DNA recognition mode may surmount the limitations of nucleic acid dyes in biological applications.

Wash-free cell imaging

The half inhibitory concentrations (IC_{50}) of **DPP-F32** and **DPP-F34** to HeLa cells determined by CCK-8 were 35.74 and 52.32 μM (Fig. S33), respectively. To minimize potential harm to the cells, a concentration of 10 μM was selected as the primary experimental concentration. Flow cytometry and confocal laser scanning microscopy (CLSM) were then employed to investigate cellular uptake and subcellular localization *via* dual channels (visible and NIR). As illustrated in Fig. 3A, B, S34, and S35, the mean intensity at 690 nm of **DPP-F32** and **DPP-F34** incubated with HeLa cells increased in a time-dependent manner but reached a plateau after 24 hours, indicating that cellular uptake had reached equilibrium at this point. However, the change at 585 nm was small, suggesting that it was difficult for live cells to activate *anti*-Kasha emission. To confirm the subcellular distribution of these two compounds, co-localization experiments were conducted using four commercial subcellular organelle-specific probes, namely Hoechst 33342, Golgi-Tracker, ER-Tracker, and Lyso-Tracker (Fig. 3C and S36). Despite the excellent DNA binding ability in solution, colocalization experiments revealed that **DPP-F32** and **DPP-F34** did not target the nucleus in living cells, with Pearson's correlation coefficients (PCCs) as low as 0.21 and 0.16, respectively. Similarly, these compounds also exhibited limited colocalization with Lyso-Tracker and ER-Tracker, displaying PCCs of 0.50 and 0.40 for **DPP-F32**, and 0.46 and 0.37 for **DPP-F34**, respectively. In

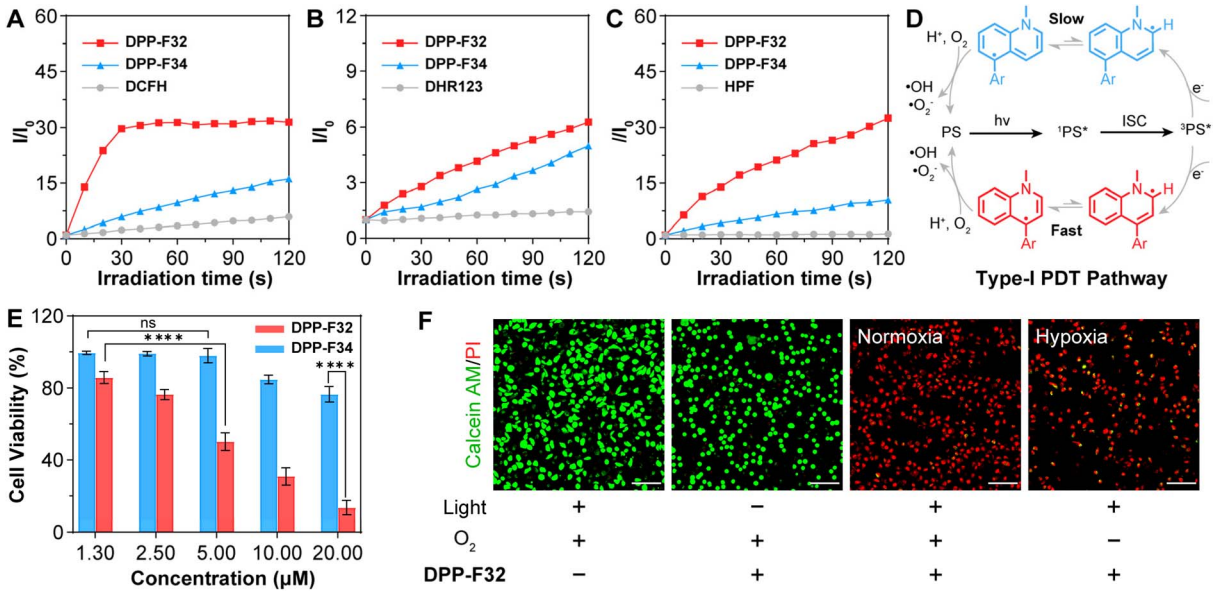

Fig. 4 (A) Comparison of the FL intensity ratio (I/I_0) at 525 nm of DCFH alone and DCFH with PS upon irradiation. (B) Comparison of the I/I_0 at 525 nm of DHR123 alone and DHR123 with PS for $^{\bullet}O_2^-$ detection upon irradiation. (C) Comparison of the I/I_0 at 515 nm of HPF alone and HPF with PS for $^{\bullet}OH$ detection upon irradiation. (D) Plausible mechanism for the type-I PDT pathway. (E) Cell viability of HeLa cells stained with various concentrations of **DPP-F32** or **DPP-F34** exposed to irradiation for 10 minutes under normoxic conditions (*t*-tests, $n = 5$, mean ± SD, $^*p < 0.05$, $^{**}p < 0.01$, $^{***}p < 0.001$, $^{****}p < 0.0001$). (F) Calcein-AM/PI co-staining imaging of HeLa cells stained with **DPP-F32** (10 μM) under different conditions. Scale bar: 100 μm. Light source: 660 nm laser (100 mW cm^{-2}).

contrast, the PCCs for colocalization with Golgi-Tracker were significantly higher, with values of 0.81 and 0.90 for **DPP-F32** and **DPP-F34**, respectively, indicating that these compounds predominantly localized to the Golgi apparatus in living cells. Given their structural similarity and identical positive charge, **DPP-F32** and **DPP-F34** exhibited comparable organelle-targeting abilities in live cells. The Golgi apparatus plays a crucial role in transporting and secreting important proteins such as cyclooxygenase-2 (COX-2) and other enzymes in cancer cells.[49] To elucidate the mechanism of Golgi apparatus specificity, molecular docking studies were conducted to investigate the specific binding of **DPP-F32** or **DPP-F34** to COX-2 (PDB: 3nt1). As shown in Fig. S37, S38, and Table S4, the docking results indicated that **DPP-F32** and **DPP-F34** could penetrate into the hydrophobic cavity of COX-2, with the binding energies of −10.04 kcal mol^{-1} and −10.18 kcal mol^{-1}, respectively. Owing to the hindering effect of the nuclear membrane, **DPP-F32** and **DPP-F34** were preferentially adsorbed onto COX-2, whose hydrophobic cavity immobilized the vinyl DPP moiety, thereby facilitating the enhancement of NIR emission.

The two compounds only exhibited single-channel imaging in living cells, prompting us to investigate their behaviors in dead cells. Apoptosis is a prevalent form of programmed cell death and the primary mechanism by which PDT induces cell death.[50] In this study, HeLa cells were subjected to oxidative stress and UV stimulation, two widely used methods for inducing apoptosis. As displayed in Fig. 3D, compared with living cells, visible emission was clearly observed in the nuclei of dead cells after **DPP-F32** staining. Specifically, in HeLa cells treated with oxidative stress, the residual cytoplasm and nucleolus displayed faint NIR emission. Meanwhile, following the UV stimulation, HeLa cells retained a relatively intact cytoplasmic matrix, with clear dual staining by a single probe observed: NIR emission brightened the cytoplasm, while the visible emission lit up the nucleus. In sharp contrast, **DPP-F34** exhibited only limited ability to illuminate the nucleus in both the cells subjected to oxidation stress and the UV-induced apoptotic cells (Fig. 3E). This might be because **DPP-F34** has a higher binding affinity for COX-2 compared to DNA, and once it is ensnared by free COX-2, release becomes difficult. These results demonstrated that the dual-emissive **DPP-F32** is capable of effectively distinguishing living and dead cells by fluorescing in the cytoplasm with NIR emission and illuminating the nucleus of dead cells with visible emission.

In vitro photodynamic properties

Considering their superior water dispersity and high molar absorption coefficients at 660 nm, the photogenerated ROS performance of **DPP-F32** and **DPP-F34** in PBS buffer was studied under 660 nm laser irradiation (100 mW cm^{-2}). The total ROS production capability, singlet oxygen ($^1O_2$) generation capacity, superoxide anion radical ($^{\bullet}O_2^-$) production ability, and hydroxyl radical ($^{\bullet}OH$) generation ability were assessed using 2′,7′-dichlorohydrofluorescein (DCFH), 9,10-anthracenediyl-bis(methylene)dimalonic acid (ABDA), dihydrorhodamine 123 (DHR123), and hydroxyphenyl fluorescein (HPF), respectively (Fig. S39). After two minutes of irradiation, the absorption intensity of ABDA remained almost unchanged both with and without PSs, indicating that neither **DPP-F32** nor **DPP-F34** exhibited significant $^1O_2$ generation. However, the FL intensity

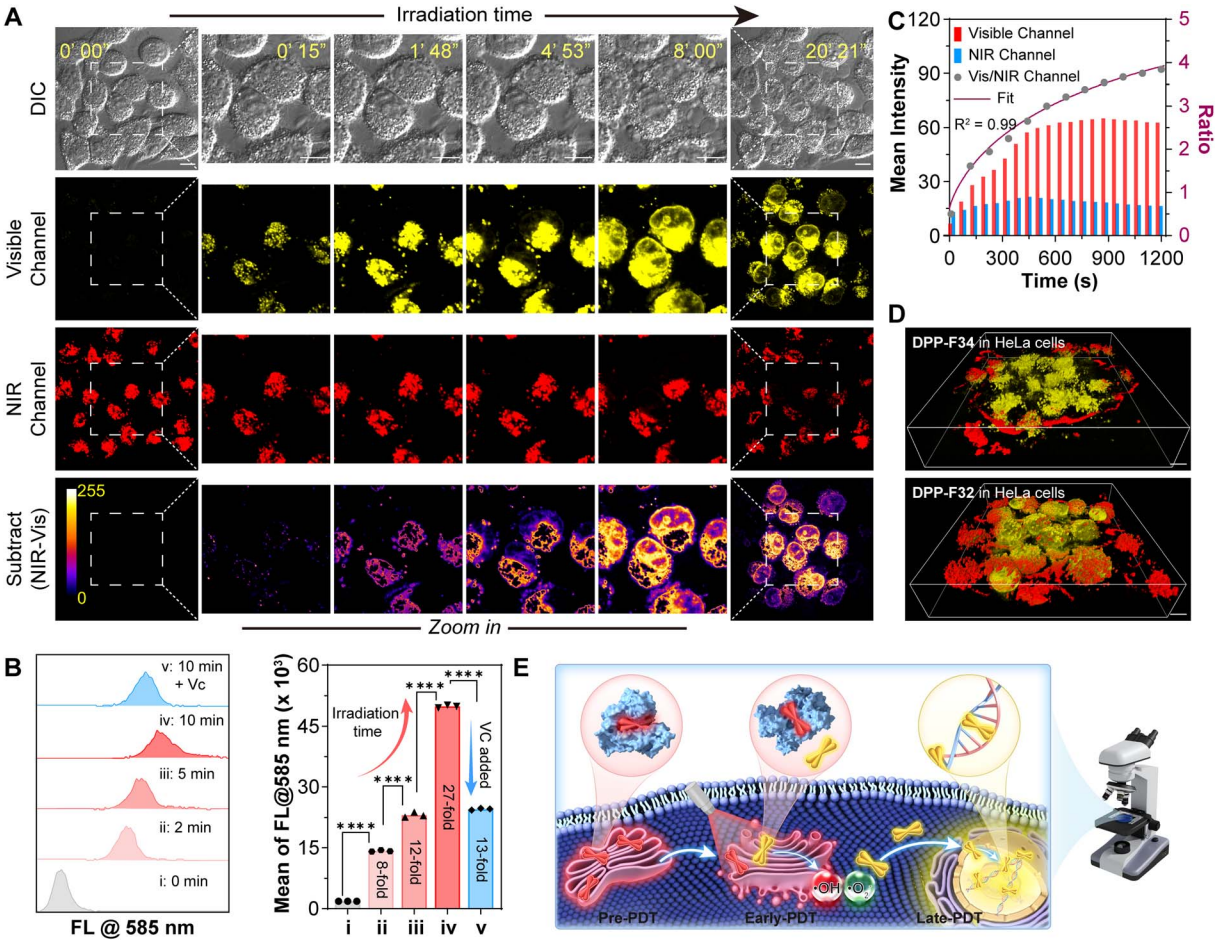

Fig. 5 (A) CLSM images of HeLa cells stained with **DPP-F32** (10 μM) under light irradiation (the light is from the laser of a confocal microscope; scanning interval: 15 seconds per picture; scan size: 512 × 512). Scale bar: 10 μm. (B) Flow cytometry analysis of FL intensity at 585 nm in HeLa cells stained with **DPP-F32** under different conditions, as well as the mean of FL intensity at 585 nm (*t*-tests, $n = 3$, *$p < 0.05$, **$p < 0.01$, ***$p < 0.001$, ****$p < 0.0001$). (C) The time-dependent emission intensities of the visible (red) and near-infrared (blue) light channels, and the ratio of visible to NIR intensities, as well as the fitting curve. (D) 3D confocal images of HeLa cells stained with **DPP-F32** or **DPP-F34** after 20 minutes of light exposure. Scale bar: 10 μm. (E) The dual-emissive self-reporting mechanism of **DPP-F32** for PDT in HeLa cells.

of DCFH increased upon irradiation in the presence of **DPP-F32** or **DPP-F34**, suggesting their capability to produce total ROS. As expected, the FL intensities of DHR123 and HPF were significantly enhanced after the addition of **DPP-F32** and **DPP-F34**, confirming their ability to generate $^{\cdot}O_2^-$ and $^{\cdot}OH$ (type-I ROS). Moreover, the detection results obtained by three indicators showed that the ROS (including total ROS, $^{\cdot}O_2^-$, and $^{\cdot}OH$) generation capacity of **DPP-F32** was superior to that of **DPP-F34** (Fig. 4A–C).

To uncover the underlying cause of the difference in the ROS production of these two isomers, theoretical calculations were conducted. The energy gaps (ΔE_{ST}) between the S_1 and the T_2 states for **DPP-F32** and **DPP-F34** were equal, which were calculated to be 0.14 eV (Fig. S40). Owing to the larger SOC constant ξ (S_1, T_2) of **DPP-F32**, a larger intersystem crossing rate constant (k_{ISC}) was derived, which was 2.7 times higher than that of **DPP-F34**. Furthermore, it was discovered that **DPP-F32** produced more carbon radical signals compared to **DPP-F34** when 5,5-dimethyl-1-pyrroline *N*-oxide (DMPO) was used as a free radical indicator (Fig. S41). Accordingly, we speculated that *para*-substituted methylquinolinium had a more efficient electron transfer pathway that promotes $^{\cdot}O_2^-$, and $^{\cdot}OH$ generation (Fig. 4D).

To evaluate the intracellular ROS generation ability of **DPP-F32** and **DPP-F34** in HeLa cells under laser irradiation, we utilized 2′,7′-dichlorodihydrofluorescein diacetate (DCFH-DA) as the ROS indicator. As shown in Fig. S42, a bright green FL signal was clearly observed within cells stained with DCFH-DA upon 660 nm laser irradiation (100 mW cm^{-2}) for 10 minutes, indicating that **DPP-F32** possessed superior intracellular ROS production capability compared to **DPP-F34**. As manifested by Fig. 4E, both **DPP-F32** and **DPP-F34** demonstrated dose-dependent photocytotoxicity against HeLa cells, with IC_{50} values of 5.34 μM and 37.13 μM, respectively. It means that **DPP-F32** had a profoundly higher photoactivated cell-killing effect than **DPP-F34**. The phototoxicity of **DPP-F32** under hypoxic conditions was evaluated using CCK-8 assays and live/dead cell staining with Calcein-AM (green fluorescence for live cells) and

propidium iodide (PI, red fluorescence for dead cells). Under hypoxic conditions, a dose-dependent cell death pattern similar to that obtained under normoxic conditions was observed, with an IC_{50} value of 5.60 μM, suggesting that the photogenerated ROS performance of **DPP-F32** was minimally affected by O_2 concentration (Fig. 4F, S43, and S44). Taken together, these results suggested that **DPP-F32** is an effective type-I PS.

Dynamic self-reporting of PDT

Building on the above findings, we further explored the potential of **DPP-F32** and **DPP-F34** to monitor real-time cell death dynamics during PDT, with experimental results systematically presented in Fig. 5A and S45. As expected, dual-channel CLSM images revealed that only the Golgi apparatus was lit up by NIR emission, while the nucleus remained dark after HeLa cells were incubated with **DPP-F32** and **DPP-F34** for 24 hours. The middle section of the scanning area was then zoomed in, and continuous irradiation with the confocal laser was applied to simulate the PDT process. Simultaneously, a series of images was captured every 15 seconds to monitor the fluorescence changes. Notably, within 15 seconds, visible emission of **DPP-F32** was activated, attributed to the ROS-induced protein denaturation. As can be seen from the magnified images, the visible emission steadily increased over time, expanding its luminescence region beyond that of the NIR region and translocating from the Golgi apparatus to the nucleus. In contrast, unirradiated cells exhibited only weak visible emission, indicating that the increase of visible emission was light-dependent. Bright-field images of **DPP-F32** staining showed that cells underwent morphological changes indicative of cell death, including shrinkage and blistering, as the irradiation time increased, further confirming that the extent of cell death correlated with irradiation duration. Under identical treatment conditions, no similar phenomenon was observed for **DPP-F34**, likely due to its low phototoxicity and weak DNA binding ability. To confirm that the FL in the visible channel originates from the PDT process rather than the physical effects of the laser, we collected quantitative data in the visible region after laser irradiation for different durations (2, 5, and 10 minutes), as well as after incubation with vitamin C (VC, a ROS inhibitor) and irradiation for 10 minutes using flow cytometry (Fig. 5B). The FL intensity at 585 nm increased in a time-dependent manner, consistent with the CLSM data, while VC-pretreated cells exhibited marked suppression, with the FL signal being 13-fold higher than those of the non-irradiated controls. The above results show that the changes in visible emission are closely related to the production of ROS.

Subsequently, the changes in both the visible and NIR channels of CLSM images were quantified (Fig. 5C). The intensity of the NIR channel decreased slightly after being irradiated for 450 seconds, indicating that **DPP-F32** dissociated from COX-2 due to protein denaturation caused by the accumulation of free radicals. The intensity of the visible light channel did not increase significantly after 750 seconds of laser irradiation, suggesting that the translocation process from the Golgi apparatus to the nucleus was ongoing. The fitted curve of the ratio (visible/NIR channel) offered a more intuitive and more accurate illustration of the dynamic process of PDT: (1) there is a sharp increase in the time range of 0 to 450 seconds, indicative of the early cell apoptosis; (2) the rate of increase decelerated between 450 and 900 seconds, suggestive of late cell apoptosis; (3) the increase rate become highly retarded between 900 and 1200 seconds, marking the endpoint of PDT. Such a strong nonlinear correlation with illumination time (R^2 = 0.99) could be utilized to generate a calibration curve to monitor PDT dynamic processes and determine the endpoint of apoptosis by virtue of reliable ratiometric imaging. Furthermore, based on the two-dimensional imaging, three-dimensional CLSM imaging was conducted. As shown in Fig. 5D, the three-dimensional images of **DPP-F34**-stained cells showed poor resolution, and **DPP-F34** did not light up the nucleus.

In particular, the three-dimensional images of **DPP-F32**-stained cells exhibited that the visible emission illuminated the nuclei overlaying the NIR emission, whereas the unirradiated cells mainly showed NIR emission. Together with the analysis of two-dimensional images, the visible emission at the three-dimensional imaging level could reflect the diffusion range of ROS as well as the area of cellular damage, indicating that **DPP-F32** holds the ability to monitor PDT in real time at a three-dimensional level.

Based on the above results, we extrapolated that **DPP-F32**, as a self-reporting PS, operated through the following mechanism (Fig. 5E): prior to the initiation of PDT, **DPP-F32** localizes at the Golgi apparatus of cancer cells with NIR emission; during the early phase of PDT, free radicals generated by **DPP-F32** under photoirradiation induce denaturation of adjacent proteins and trigger the visible emission; in the late phase of PDT, **DPP-F32** translocates to the nucleus from the proteins, binds to DNA, and then enables the nuclear visualization through bright visible emission.

Conclusions

In summary, based on the gradient D–A molecular engineering strategy, we successfully developed two dual-emissive PS isomers, *i.e.*, **DPP-F32** and **DPP-F34**, where the divinyl-substituted DPP moiety serves as the core electron acceptor, the TPA units act as the electron donors, and the methylquinolinium groups function as the additional electron acceptors. Comparative study on the introduction of two positionally isomeric additional electron-acceptors, *i.e.*, *para*- and *meta*-substituted methylquinolinium units, revealed that the *para*-substituted isomer exhibited enhanced performance in this strategy, attributed to a stronger local electron push–pull effect. Moreover, the twisted triphenylamine unit effectively decoupled the charge transfer between the core electron acceptor and additional acceptor, thereby preserving their respective functions and photophysical properties. Notably, the TPA-divinyl-decorated DPP fragment exhibited viscosity responsiveness with NIR emission enhanced upon viscosity increase, while the methylquinolinium-TPA promoted the S_2-to-S_0 excited-state decay with the visible emission enhanced upon DNA binding.

In addition, **DPP-F32** with the *para*-substituted methylquinolinium was more favorable for the type-I PDT pathway due to its more efficient electron transfer pathway and larger SOC constant. Importantly, **DPP-F32** not only demonstrated a remarkable ability to distinguish live and dead cells but also achieved dual-emissive ratiometric monitoring of the PDT process at both two- and three-dimensional levels.

This work provides inspiration for the development of novel *anti*-Kasha fluorescent molecules, where the combination of new forms of primary and additional electron acceptors will burst with new vigor. Moreover, it has opened up new avenues for the development of *anti*-Kasha PSs and laid a solid foundation for the advancement of next-generation PSs with real-time therapeutic feedback capabilities. Such intelligent PSs are expected to bridge the gap between therapeutic intervention and diagnostic monitoring, thereby promoting the development of personalized cancer theranostics. Our future research will focus on optimizing these compounds for clinical translation, exploring synergistic effects with other therapeutic modalities, and evaluating their long-term safety and efficacy *in vivo*. It can be anticipated that these innovations will contribute to the field of precision medicine, enhancing patient outcomes and paving the way for more effective cancer treatments.

Author contributions

Xixin Gu: conceptualization, data curation, formal analysis, investigation, methodology, visualization, writing–original draft. Xinyi Zhang: data curation, methodology, software, validation, visualization. Yujie Han: investigation, validation. Ju Mei: project administration, resources, software, writing – review & editing. Qi-Wei Zhang: funding acquisition, resources, writing – review & editing. Jianli Hua: conceptualization, investigation, methodology, project administration, funding acquisition, writing – review & editing.

Conflicts of interest

There are no conflicts to declare.

Data availability

The data that support the findings of this study are available from the corresponding author upon reasonable request.

Materials and methods, detailed synthesis and characterization of the synthesized compounds, spectral tests, and confocal imaging are provided in the SI accompanying this article. See DOI: **https://doi.org/10.1039/d5sc03880d**.

Acknowledgements

For financial support of this research, the authors thank the projects supported by the National Natural Science Foundation of China (21788102, 22271093, 21971064 and 22322405), the Science and Technology Commission of Shanghai Municipality (24DX1400200), the Programme of Introducing Talents of Discipline to Universities (B16017) and the Fundamental Research Funds for the Central Universities. The authors thank the Research Center of Analysis and Test of East China University of Science and Technology for the help on the characterization.

Notes and references

1 T. J. Dougherty, C. J. Gomer, B. W. Henderson, G. Jori, D. Kessel, M. Korbelik, J. Moan and Q. Peng, *J. Natl. Cancer Inst.*, 1998, **90**, 889–905.
2 D. E. Dolmans, D. Fukumura and R. K. Jain, *Nat. Rev. Cancer*, 2003, **3**, 380–387.
3 X. Li, J. F. Lovell, J. Yoon and X. Chen, *Nat. Rev. Clin. Oncol.*, 2020, **17**, 657–674.
4 W. Fan, P. Huang and X. Chen, *Chem. Soc. Rev.*, 2016, **45**, 6488–6519.
5 X. Zhao, J. Liu, J. Fan, H. Chao and X. Peng, *Chem. Soc. Rev.*, 2021, **50**, 4185–4219.
6 M. Dirak, C. M. Yenici and S. Kolemen, *Coord. Chem. Rev.*, 2024, **506**, 215710.
7 G. Feng, G.-Q. Zhang and D. Ding, *Chem. Soc. Rev.*, 2020, **49**, 8179–8234.
8 Z. Zhang, M. Kang, H. Tan, N. Song, M. Li, P. Xiao, D. Yan, L. Zhang, D. Wang and B. Z. Tang, *Chem. Soc. Rev.*, 2022, **51**, 1983–2030.
9 A. Sharma, P. Verwilst, M. Li, D. Ma, N. Singh, J. Yoo, Y. Kim, Y. Yang, J.-H. Zhu, H. Huang, X.-L. Hu, X.-P. He, L. Zeng, T. D. James, X. Peng, J. L. Sessler and J. S. Kim, *Chem. Rev.*, 2024, **124**, 2699–2804.
10 T. Lammers, S. Aime, W. E. Hennink, G. Storm and F. Kiessling, *Acc. Chem. Res.*, 2011, **44**, 1029–1038.
11 H. Chen, W. Zhang, G. Zhu, J. Xie and X. Chen, *Nat. Rev. Mater.*, 2017, **2**, 17024.
12 A. Dasgupta, I. Biancacci, F. Kiessling and T. Lammers, *Theranostics*, 2020, **10**, 956–967.
13 P. J. Gawne, F. Man, P. J. Blower and R. T. M. De Rosales, *Chem. Rev.*, 2022, **122**, 10266–10318.
14 S. P. Rowe and M. G. Pomper, *Ca-Cancer J. Clin.*, 2022, **72**, 333–352.
15 X. Ma, M. Mao, J. He, C. Liang and H.-Y. Xie, *Chem. Soc. Rev.*, 2023, **52**, 6447–6496.
16 J. Wang, X. Zhao, X. Zhu, S. Wang, X. Sun, Q. Zhang, X. Chen, A. Wang, M. Yang and H. Zhou, *Anal. Chem.*, 2024, **96**, 19404–19413.
17 Y. Chen, T. Xiong, Q. Peng, J. Du, W. Sun, J. Fan and X. Peng, *Nat. Commun.*, 2024, **15**, 6935.
18 Y. Xu, J. Zhang, Z. Wang, P. Zhang, Z. Zhang, Z. Yang, J. W. Y. Lam, R. T. K. Kwok, L. Meng, D. Dang and B. Z. Tang, *Biomaterials*, 2025, **314**, 122847.
19 T. Zhang, Y. Li, Z. Zheng, R. Ye, Y. Zhang, R. T. K. Kwok, J. W. Y. Lam and B. Z. Tang, *J. Am. Chem. Soc.*, 2019, **141**, 5612–5616.
20 H. Zou, S. Gan, H. Shen, B. He, Z. Zheng, J. Li, J. C. Huang, L. Zheng, B. Z. Tang and J. Zhang, *Mater. Today*, 2022, **61**, 117–128.
21 H.-H. Han, H. Tian, Y. Zang, A. C. Sedgwick, J. Li, J. L. Sessler, X.-P. He and T. D. James, *Chem. Soc. Rev.*, 2021, **50**, 9391–9429.

22 Z. Wang, Y. Jiang, Q. Zhang, Q. Lu, Q. Wang, G. Zheng, J. Niu and M. Tian, *Sens. Actuators, B*, 2024, **401**, 135072.
23 M. Tian, Y. Ma and W. Lin, *Acc. Chem. Res.*, 2019, **52**, 2147–2157.
24 X. Chen, Q. Yang, X. Lv, Y. Xiong, B. Z. Tang and X. Huang, *Coord. Chem. Rev.*, 2024, **516**, 215970.
25 R. Gui and H. Jin, *J. Photochem. Photobiol., C*, 2024, **58**, 100650.
26 R. Gui, H. Jin, X. Bu, Y. Fu, Z. Wang and Q. Liu, *Coord. Chem. Rev.*, 2019, **383**, 82–103.
27 X. Huang, J. Song, B. C. Yung, X. Huang, Y. Xiong and X. Chen, *Chem. Soc. Rev.*, 2018, **47**, 2873–2920.
28 S. K. Behera, S. Y. Park and J. Gierschner, *Angew. Chem., Int. Ed.*, 2021, **60**, 22624–22638.
29 H. Sun, S. Shen, C. Li, W. Yu, Q. Xie, D. Wu and L. Zhu, *Adv. Funct. Mater.*, 2025, **35**, 2415400.
30 M. Kasha, *Discuss. Faraday Soc.*, 1950, **9**, 14–19.
31 A. P. Demchenko, V. I. Tomin and P.-T. Chou, *Chem. Rev.*, 2017, **117**, 13353–13381.
32 K. Veys and D. Escudero, *Acc. Chem. Res.*, 2022, **55**, 2698–2707.
33 L. Yu, Y. Liu, D. Zhou, Z. Ni, S. Li and C. Yang, *Aggregate*, 2025, **6**, e70075.
34 K. Wang, X. Ou, X. Niu, Z. Wang, F. Song, X. Dong, W. Guo, H.-Q. Peng, Z. Zhao, J. W. Y. Lam, J. Sun, H. Wu, S.-Y. Yu, F. Li and B. Z. Tang, *Aggregate*, 2025, **6**, e667.
35 H. Wang, J. Wang, T. Zhang, Z. Xie, X. Zhang, H. Sun, Y. Xiao, T. Yu and W. Huang, *J. Mater. Chem. C*, 2021, **9**, 10154–10172.
36 L. Shi, C. Yan, Z. Guo, W. Chi, J. Wei, W. Liu, X. Liu, H. Tian and W.-H. Zhu, *Nat. Commun.*, 2020, **11**, 793.
37 J. Gong, P. Wei, J. Liu, Y. Chen, Z. Zhao, W. Zhao, H. Xie, C. Ma, J. W. Y. Lam, K. S. Wong, Y. Li and B. Z. Tang, *Aggregate*, 2023, **4**, e265.
38 P. Chen, G. Shan, Q. Nie, Y. Yan, P. Zhang, Z. Zhao, H.-T. Feng and B. Z. Tang, *Sci. China Chem.*, 2024, **67**, 1740–1752.
39 F. Hu, S. Xu and B. Liu, *Adv. Mater.*, 2018, **30**, 1801350.
40 S. Xu, Y. Duan and B. Liu, *Adv. Mater.*, 2020, **32**, 1903530.
41 L. Feng, C. Li, L. Liu, Z. Wang, Z. Chen, J. Yu, W. Ji, G. Jiang, P. Zhang, J. Wang and B. Z. Tang, *ACS Nano*, 2022, **16**, 4162–4174.
42 L. Feng, C. Li, L. Liu, X. Chen, G. Jiang, J. Wang and B. Z. Tang, *Angew. Chem., Int. Ed.*, 2022, **61**, e202212673.
43 Y. Gao, X. Wang, X. He, Z. He, X. Yang, S. Tian, F. Meng, D. Ding, L. Luo and B. Z. Tang, *Adv. Funct. Mater.*, 2019, **29**, 1902673.
44 Y. Gao, Z. He, X. He, H. Zhang, J. Weng, X. Yang, F. Meng, L. Luo and B. Z. Tang, *J. Am. Chem. Soc.*, 2019, **141**, 20097–20106.
45 K. Wang, L. Liu, D. Mao, M. Hou, C. Tan, Z. Mao and B. Liu, *Angew. Chem., Int. Ed.*, 2022, **134**, e202114600.
46 X. Liu, H. Li, G. Qi, Y. Qian, B. Li, L. Shi and B. Liu, *J. Am. Chem. Soc.*, 2024, **146**, 31656–31664.
47 J. Liu, W. Zhang, C. Zhou, M. Li, X. Wang, W. Zhang, Z. Liu, L. Wu, T. D. James, P. Li and B. Tang, *J. Am. Chem. Soc.*, 2022, **144**, 13586–13599.
48 B. Li, C. Bian, L. Yang, Y. Zhu, Z. Li and M. Yu, *Anal. Chem.*, 2024, **96**, 14044–14052.
49 Y. Luo, S. Zhang, H. Wang, Q. Luo, Z. Xie, B. Xu and W. Tian, *CCS Chem.*, 2022, **4**, 456–463.
50 Z. Zhou, J. Song, L. Nie and X. Chen, *Chem. Soc. Rev.*, 2016, **45**, 6597–6626.